Polyacrylonitrile/Carbon Nanotube Composite Films

Huina Guo, Marilyn L. Minus,† Sudhakar Jagannathan, and Satish Kumar*

The School of Polymer, Textile and Fiber Engineering, Georgia Institute of Technology, Atlanta, Georgia 30332

ABSTRACT Reinforcement efficiency of different types of carbon nanotubes (CNT) have been compared in polyacrylonitrile (PAN) films at nanotube loadings of 5, 10, and 20 wt %. The films are characterized for mechanical, dynamic-mechanical, and thermomechanical properties, electrical conductivity, as well as structural analysis. PAN/CNT composite films exhibit electrical conductivities up to 5500 S/m. Based on X-ray diffraction, PAN crystallinity was shown to increase with the presence of CNT. PAN−CNT interactions in the various composites were compared using conventional activation energy analysis. The strongest physical interaction between PAN and CNT was found in samples containing single-wall carbon nanotubes (SWNT). CNT surface area was also measured using nitrogen gas adsorption and correlated with PAN−CNT composite film mechanical properties, in an effort to better understand PAN−CNT interactions for different CNT morphologies. Solvent behavior of various composite films has also been investigated. The presence of CNT was found to improve PAN solvent resistance.

KEYWORDS: polyacrylonitrile • carbon nanotubes • interaction • surface area • composite

INTRODUCTION

Structure−property relationships in polymer/carbon nanotube (CNT) composite materials are influenced by many factors, including (i) polymer matrix−CNT interactions (1−6); (ii) overall dispersion quality, exfoliation, and orientation of CNT (1, 4, 7−9); (iii) diameter, type, and morphology of CNT (10−12); as well as (iv) various loadings of CNT in the matrix (13). Though the body of literature focused on characterization of polymer/CNT composites for various applications is extensive (14−17), a large number of these studies concentrate only on understanding the effect of individual factors on the properties of these nanocomposites. Several studies have also summarized the work on polymer/CNT composites, showing advancements in mechanical (9, 18−20), electrical (21−23), and optical properties (24, 25), dispersion of CNT in polymer matrices (9, 26), as well as the overall challenges for processing of polymer/CNT nanocomposites (27, 28). Some studies on mechanical property enhancement in polymer/CNT composites have focused on orientation and dispersion of CNT (1, 4, 29); the affect of surface area and size of CNT (10, 11); CNT loading in polymer matrices; as well as interfacial interaction between the polymer and CNT (1, 4, 15, 30).

Polyacrylonitrile (PAN) is an important polymeric material because of its use as a precursor for carbonaceous materials, including carbon fibers (31, 32) and porous/activated carbon materials for electrode (33, 34) and for nanofiber processing for some biological applications (35, 36). Several studies have reported PAN/CNT films and fibers with improved mechanical properties due to good interaction between PAN and CNT (11, 37, 38). Recent work has detailed the processing of PAN/CNT composite fibers for next-generation carbon fiber production (1, 2, 39), as well as PAN/CNT films and fibers for electrochemical supercapacitor applications (33, 34, 40−42). Although there has been a body of work dedicated to PAN/CNT composite fibers that include conventionally spun (i.e., solution, gel, and dry-jet wet spinning) (1, 2, 11, 37, 39, 43) and electro-spun (44, 45) fibers, up to this point, only limited studies exist on PAN/CNT composite films (38, 46−51). Studies on PAN/multiwall carbon nanotube (MWNT) films show that at nanotube loadings ranging from 1 to 25 wt % uniform dispersion of MWNT was achieved (52, 53). In addition, previous work form our group also shows that PAN composite films could also be fabricated using singe-wall carbon nanotubes (SWNT) and vapor grown carbon nanofibers (VGCNF) (46, 47) with uniform dispersion, improvements in mechanical and electrical properties, and enhancements in PAN crystallization and dimension stability. So far, PAN composite films produced using CNT show the potential to disperse nanotubes well throughout the matrix and improve various properties for many potential applications.

Toward the efforts for deeper understanding of processing PAN/CNT composites, in this work the influence of CNT type, morphology, impurity level, and loading in the PAN matrix are all investigated. In previous work, similar studies were performed on poly(methyl methacrylate)/SWNT composite films for high SWNT loadings (up to 15 wt %) of different impurity levels (metallic impurity up to 35 wt %) (54). In this work, PAN/CNT films at various nanotube loadings (i.e., 5, 10, and 20 wt %) were fabricated. The reinforcement efficiency of different types of CNT including, SWNT, double-wall carbon nanotubes (DWNT), MWNT, and VGCNF have been compared in PAN films, and mechanical

* Corresponding author. E-mail: satish.kumar@ptfe.gatech.edu. Tel.: (404) 894-7550. Fax: (404) 894-8780.

Received for review December 16, 2009 and accepted April 21, 2010

† Current address: Department of Mechanical and Industrial Engineering, Northeastern University, Boston, MA 02115.

DOI: 10.1021/am100155x

and electrical property and morphology characterizations were performed on composite films. These characterizations are used to investigate the roles that CNT-PAN interaction, as well as CNT surface area and structure play toward property changes observed in composite properties as compared to control films.

EXPERIMENTAL SECTION

Five batches of SWNT (SWNT1: Lot X-5054C (3 wt % metallic impurity); SWNT2, Lot XO-0PPP (1 wt % metallic impurity); SWNT3, Lot XO-1PPP (1 wt % metallic impurity); SWNT4, Lot P-0252 (6 wt % metallic impurity); and SWNT5, Lot R-0231 (35 wt % metallic impurity) were obtained from Carbon Nanotechnologies, Inc. (Houston, TX). DWNT (Batch 270c700056, 5 wt % catalytic impurity) was obtained from Nanocyl, Co. (Belgium), MWNT (3 wt % catalytic impurity) from Iljin Nanotech, Co. (Korea), and VGCNF (Batch PR24-HHT-LD2850, 0.3 wt % impurity) from Applied Sciences, Inc. (Cedarville, OH). The catalytic impurity of the each type of nanotube was determined from the thermogravimetric analysis (TGA) based on the residual weight. PAN (M_w 100 000 g/mol) containing 6.7% methyl acrylate random comonomer was obtained from Japan Exlan Company. Dimethylformamide (DMF) was purchased from Sigma-Aldrich and used as-received.

Carbon nanotubes and VGCNF were added to 50 mL of DMF and sonicated (Fisher FS30 bath sonicator, frequency 43 kHz, power 150 W) for 48 h (DWNT was sonicated for 6 days) until an optically homogeneous dispersion was formed. The homogeneity of dispersion was confirmed by optical microscopy to ensure that no large chunks were present in the nanotube dispersion. In previous work, UV−vis spectroscopy has been used to analyze CNT dispersions in DMF and have shown that stable uniform dispersions are achievable (55). Two-hundred-forty to three-hundred milliograms PAN was added to the CNT/DMF dispersion homogenized and dissolved while stirring. Excess solvent was evaporated to obtain the final solution volume of 25 mL. PAN/CNT/DMF solutions analyzed by optical microscopy appeared homogeneous at this scale. The PAN/CNT/DMF solution was cast on a glass substrate and kept in a vacuum oven at 80 °C for 3 days for solvent removal to form the film. PAN/CNT composite films with thickness ~25 μm containing various loadings of CNT (5, 10, and 20 wt %) were all prepared by the same procedure.

Thermogravimetric analysis (TGA) of CNT powders was conducted on TGA 2950 (manufactured by TA Instruments, Inc.) in air at a heating rate of 10 °C/min. Raman spectra were collected using a Holoprobe Research Raman Microscope equipped with a 785 nm excitation laser (made by Kaiser Optical System Inc.). For porosity and Brunauer−Emmett−Teller (BET) surface area measurements, the isothermal N_2 gas adsorption and desorption at 77 K were carried out on ASAP 2020 (manufactured by Micromeritics Inc.), on samples degassed at 90 °C for 16 h. Wide-angle X-ray diffraction was performed using a MicroMax002 WAXS/SAXS source (λ ~0.15418 nm) equipped with 2D R-axis V^{++} detector system (manufactured by Rigaku/MSC Inc.). Scanning electron microscopy (SEM) was performed on a LEO1530 field-emission microscope (operating voltage 10 to 16 kV). High-resolution transmission electron microscopy (HR-TEM) was performed on a Hitachi HF-2000 transmission electron microscope operated at 200 kV. Thermal mechanical analysis and coefficient of thermal expansion (CTE) was determined using a thermo-mechanical analyzer (TMA) (manufactured by TA Instruments, model TMA 2940) at 0.05 MPa prestress (film dimensions: 10 mm long by 2 mm wide; 4 to 6 samples were tested for each film type) during the second heating cycle using a heating rate of 5 °C/min. RSA III instrument (manufactured by Rheometrics Scientific) was used to measure tensile and dynamic mechanical properties of the films. The gauge length, film width, and strain rate for tensile tests were 20 mm, 2 mm, and 10%/min, respectively. Dynamic mechanical measurements were carried out at testing frequencies of 0.1, 1, 5, and 10 Hz at a temperature increment of 1 °C/min. Solvent resistance tests were carried out by placing the composite film in DMF at 25 °C for 1 h. In-plane dc electrical conductivity was measured by the four-probe method (manufactured by Signatone).

Table 1. Degradation Temperatures and BET Surface Area of Various Carbon Nanotubes in Air

carbon nanotube samples	initial degradation temperature (°C)	temperature at the fastest degradation rate (°C)	BET surface area (m^2/g)
SWNT1	516	550	583 ± 2
SWNT2	489	555	830 ± 6
SWNT3	483	570	795 ± 10
SWNT4	424	510	823 ± 10
SWNT5	368	421	434 ± 4
DWNT	440	456	563 ± 1
MWNT	584	640	161 ± 1
VGCNF	695	755	41 ± 1

RESULTS AND DISCUSSION

Physical Properties of CNT. For this study, the five SWNT samples as listed in the experimental section are referred to as SWNT1−SWNT5, respectively. The degradation temperature for the various CNT used were determined from TGA plots and are listed in Table 1. MWNT and VGCNF was found to degrade at higher temperatures as compared to the various SWNT and DWNT (56), which may be due to the existence of layered graphitic structures. The lower degradation temperature found for SWNT4 and SWNT5 as compared to SWNT1, SWNT2, and SWNT3 may be due to the presence of higher metal content as well as smaller tube diameter (i.e., the average diameter for SWNT4 and SWNT5 was 1 nm and that for SWNT1, SWNT2, and SWNT3 was 2 nm). An inverse relationship was observed when the degradation temperatures were plotted against the BET surface area of nanotubes (Figure 1). This analysis suggests that larger surface area may be associated with lower initiation temperature for degradation.

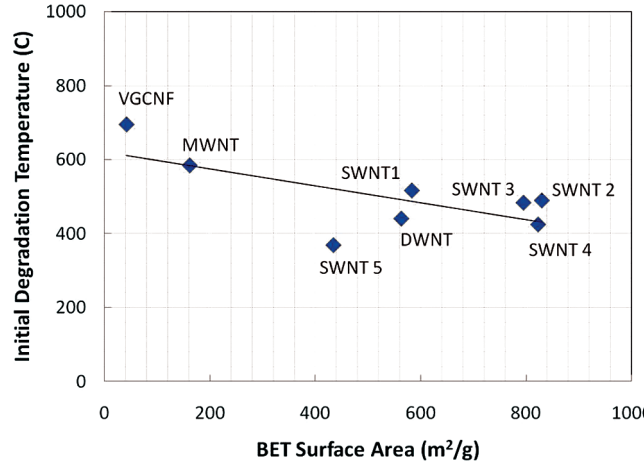

FIGURE 1. Initial degradation temperature as a function of BET surface area for various CNT.

Table 2. Summary of Wide-Angle X-ray Diffraction Results for CNT Powders

peak identity		SWNT1	SWNT2	SWNT3	SWNT4	SWNT5	DWNT	MWNT	VGCNF
(11) plane	2θ (deg)				8.14	8.02			
	d (nm)				1.085	1.101			
(10) plane	2θ (deg)				13.18	13.22			
	d (nm)				0.671	0.669			
γ-band carbon	2θ (deg)				20.74				
	d (nm)				0.428				
(002) interplanar graphitic spacing	2θ (deg)	25.92	25.97	25.86			25.44	25.88	26.30
	d (nm)	0.344	0.343	0.344			0.350	0.344	0.339
	cryst size (nm)	30	40	30			83	93	150
(100) graphite/ (110) α-Fe	2θ (deg)	43.56	43.01	43.05	43.93	44.28	43.30	42.90	42.60
	d (nm)	0.208	0.210	0.210	0.206	0.204	0.209	0.211	0.212

Morphology of the various CNT were also characterized by both transmission and scanning electron microscopy (Supporting Information Figures S1 and S2). SWNT bundle diameter was determined to be in the range of 8 to 30 nm. Due to their higher catalytic impurity content, metallic particles were clearly observed for samples SWNT4 and SWNT5. The size of the metal particles in the SWNT4 and SWNT5 are in the range of 3 to 5 nm. SWNT3 powder sample was observed to have most uniform bundle diameter distribution based on SEM observations, as well as least metal (from TGA) as compared to all other types of SWNT used in this study. The average diameter of the DWNT was found to be about 5 nm. DWNT samples used in this study tended not to form bundles but instead exist as highly entangled individual nanotubes. MWNT and VGCNF also exist as individual entangled nanotubes/fibers. VGCNFs exhibit double-layer morphology. The inner-wall of VGCNF is oriented at an angle with respect to the fiber axis, whereas the outer wall is oriented parallel to the nanofiber axis. The inner diameter is ~25 nm and the outer diameter is ~60 nm (57).

The 2θ and d-spacings values obtained from wide-angle X-ray diffraction (WAXD) for the various SWNT are listed in Table 2. All CNT powders show a characteristic peak around ~44°, which is attributed to a (100) plane in graphite (58) and/or a (110) reflection of the α-Fe body-centered cubic lattice. SWNT1, SWNT2, and SWNT3 show the peak at 25.9° attributed to (002) plane of the interplanar graphite spacings resulting from the existence of some DWNT and few-wall carbon nanotubes present along with SWNT in these batches (39). DWNT, MWNT, and VGCNF also exhibit a peak at ~25.4° to 26.3° due to the graphitic layer stacking. Ordered SWNT bundles exhibit a 2D hexagonal crystal lattice packing and show X-ray diffraction peaks at ~8 and ~13° which correspond to (10) and (11) planes (59). WAXD of SWNT4 and SWNT5 show the peaks corresponding to (10) and (11) planes. From the d-spacing for the (10) plane and assuming an intertube distance (d_i) in the SWNT bundle of 0.34 nm, the average diameter (d_t) of SWNT4 and SWNT5 is calculated using eq 1 and estimated to be 0.92 and 0.94 nm, respectively. The absence of (10) and (11) planes in the X-ray pattern of SWNT1, SWNT2, and SWNT3 further indicates disruption of these crystalline packing due to the presence of other CNT types (i.e., DWNT and few-walled carbon nanotubes) in these batches (39). The peak at ~21° 2θ for SWNT4 can be attributed to the γ-band of carbon, which arises because of the packing of saturated structures such as aliphatic carbons (60−63).

$$d_t = d_{SWNT(10)} - d_i \quad (1)$$

Raman spectra for various CNT powders were collected and the intensity in all cases is normalized with respect to the intensity of the G band (1550−1605 cm^{-1}) (see the Supporting Information, Figure S3). The peaks located in the region of ~200−500 cm^{-1} correspond to the radial breathing mode (RBM). The disorder-induced D band appears at ~1300 cm^{-1} because of the presence of disordered carbon, and SWNTs with incomplete or modified wall structure. The normalized intensity of D band for SWNT1, SWNT2, SWNT3, SWNT4, and SWNT5 is 0.2, 0.25, 0.1, 0.12, and 0.08, respectively, assuming that the intensity of G band in all cases is 1. High intensity of D band for SWNT1 and SWNT2 indicate that these nanotube samples contain more amorphous and disordered carbon among SWNT powders used in this study. The intensity of D band of both MWNT and VGCNF is also very high (2.17 and 0.99, respectively), indicating amorphous carbon and highly defective graphitic structures present in these two samples. The peak positions and the full width at half maxima (fwhm) of the G band for the higher frequency component for various CNTs are listed in Table S1 of the Supporting Information. G bands for SWNT4 and SWNT5 clearly show two peaks characteristic of metallic and semiconductive tubes present in SWNT samples as compared to SWNT1, SWNT2, and SWNT3 (samples established as a mixture of tube types) powders given in Figure 2.

Nitrogen absorption measurement results given in Table 1 show that all SWNT samples and DWNT have higher BET surface area as compared to MWNT and VGCNF. The BET surface areas for SWNT2, SWNT3, and SWNT4 are 830, 795, and 834 m^2/g, respectively, and are significantly higher than those for SWNT1 (583 m^2/g) and SWNT5 (434 m^2/g). BET surface areas for MWNT and VGCNF are 161 and 41 m^2/g, respectively. The pore volume distribution curves for all CNT samples used are also plotted in the Supporting Information, Figure S4.

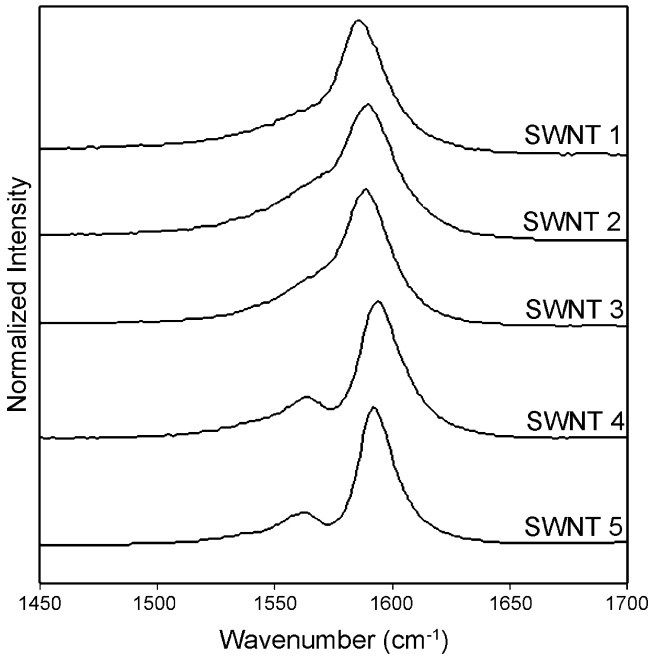

FIGURE 2. Normalized G band of Raman spectra for the various SWNT powder samples used in this study.

Mechanical and Electrical Properties of PAN/CNT Composite Films. Tensile modulus, tensile strength, elongation-at-break, and electrical conductivity values for the composites are listed in Table 3. PAN/SWNT2, PAN/SWNT3, PAN/SWNT4, PAN/VGCNF composite films with 5 wt % loading of CNT exhibit improved mechanical properties relative to the control PAN film. Among the SWNT containing composites, films prepared using SWNT3 shows the highest improvement in tensile modulus (3.7 GPa for control PAN to 5.6 GPa for PAN/SWNT3) and tensile strength (53 MPa for control PAN to 77 MPa for PAN/SWNT3). PAN/SWNT2 and PAN/SWNT4 show similar enhancement in tensile modulus (4.9 and 5.0 GPa for PAN/SWNT2 and PAN/SWNT4, respectively). The relatively lower enhancement in tensile properties for SWNT2 composite film as compared to SWNT4 may be attributed to the presence of more amorphous carbon/defective tube structures in these samples as evidenced from Raman data. Composite films prepared from SWNT1 and SWNT5 show little enhancement in tensile modulus and a decrease in tensile strength as compared to the control PAN (Table 3). One factor that may contribute to the lack of improved mechanical properties for SWNT1 and SWNT5 composites is the low surface area measured for these samples (Table 1), which would lead to reduced interfacial interaction with PAN as compared to SWNT2, SWNT3, and SWNT4. Among DWNT, MWNT, and VGCNF composites at 5 wt % CNT loading, only PAN/VGCNF composite film exhibits improvement in tensile properties (4.4 GPa tensile modulus and 80 MPa tensile strength).

Tensile modulus increases for SWNT3, SWNT4, and SWNT5 composites with 10 wt % SWNT loading (Table 3), and a significant improvement in tensile strength is observed for PAN/SWNT3 films. Overall, among various SWNT composites, the improved tensile strength of films containing SWNT2, SWNT3, and SWNT4 may be attributed to their higher surface area as compared to SWNT1 and SWNT5. With the increase in loading to 10 wt % PAN/DWNT, PAN/MWNT, and PAN/VGCNF composites, all exhibit improvement in the tensile properties as compared to the control films. In addition to films with 5 and 10 wt % CNT loading, four types of CNT (SWNT1, SWNT3, SWNT5, and VGCNF) were also used to prepare the composite films with 20 wt % loading. PAN/SWNT3 composite film shows the highest increase in modulus, and tensile strength, of 244 and 79%, respectively, whereas strain-to-break decreased by 519% as compared to the control PAN films. These tensile properties compare favorably to the values obtained with PAN/SWNT (60/40) films reported earlier (47). As expected, with increasing CNT loading, the electrical conductivity of PAN/CNT composite films also increases (Table 3). The PAN/SWNT3 films at all loadings (5, 10, and 20 wt %) exhibit the highest electrical conductivity among all composite films prepared with same loading of CNT (Table 3). The electrical conductivity of PAN/SWNT3 samples increase from 88 to 243 to 5500 S/m for the 5, 10, and 20 wt % samples, respectively. These results are higher than previously published work. PAN/MWNT electrospun mats exhibit conductivities of 20−50 S/m for samples containing up to 10 wt % CNT (64). Activated PAN/MWNT electrospun fiber mats with 3 wt % loading exhibit electrical conductivity of ~96 S/m (65). PAN/MWNT films fabricated by hot pressing of CNT coated PAN nanoparticles at 5 and 10 wt % loading show values of 3.942×10^{-1} and 2.886 S/m, respectively (66).

Improvement in tensile modulus, tensile strength, as well as electrical conductivity of polymer matrix in the presence of CNT depends on a number of factors. Interfacial interaction between CNT and polymer is one of the critical factors that can dictate the composite properties. CNT−polymer interaction depends on the interfacial area between the polymer and the CNT. As the surface area of CNT increases, the available interfacial area between the polymer and nanotube also increases which may result in better polymer−CNT interaction and consequently improved composite properties. Figure 3a shows the plot of tensile modulus of various PAN/CNT films as a function of the measured CNT BET surface area. From these plots, the general trend is that tensile modulus of the composite films improves as the CNT surface area increases. Similarly, the tensile strength of various films is also plotted as a function of CNT surface area (Figure 3b). With the exception of PAN/VGCNF films, which shows higher strength despite its low surface area at the same CNT loading, the tensile strengths of various composite films increase with increasing nanotube surface area. Improved tensile properties of PAN/VGCNF films may be attributed to the long length of VGCNF (30−100 μm), whereas the length of SWNT, DWNT, and MWNT is typically estimated to be on the order of several hundred nanometers to a few micrometers. The effect of nanotube surface area on the reinforcement efficiency has been previously studied for poly(vinyl alcohol) by Cadek (10) and for polyacrylonitrile by Chae (11). The results suggest that reinforcement scales linearly with the total nanotube surface area. The results

Table 3. Mechanical and Electrical Properties of Control PAN and PAN/CNT Composite Films

	CNT loading					
sample	(wt %)	(vol %)	modulus (GPa)	strength (MPa)	elongation (%)	conductivity (S/m)
Control PAN	0	0	2.7 ± 0.4	57 ± 4	22.3 ± 6.5	
PAN/SWNT1	5	4.6	3.8 ± 0.3	47 ± 9	1.6 ± 0.6	1.2
PAN/SWNT2	5	4.6	4.9 ± 0.1	79 ± 8	5.1 ± 1.3	6.1
PAN/SWNT3	5	4.6	5.6 ± 0.3	77 ± 3	3.9 ± 0.9	88.1
PAN/SWNT4	5	4.6	5.0 ± 0.5	70 ± 12	4.4 ± 1.4	4.1
PAN/SWNT5	5	4.6	3.9 ± 0.3	48 ± 8	2.0 ± 0.5	7.3
PAN/DWNT	5	4.0	3.5 ± 0.2	48 ± 15	1.9 ± 0.8	0.006
PAN/MWNT	5	3.3	3.4 ± 0.1	35 ± 4	1.2 ± 0.2	0.005
PAN/VGCNF	5	3.1	4.4 ± 0.3	80 ± 6	5.5 ± 1.6	0.7
PAN/SWNT1	10	9.2	3.1 ± 1.3	41 ± 17	1.7 ± 0.7	35.2
PAN/SWNT2	10	9.2	4.8 ± 0.4	72 ± 13	5.2 ± 1.6	78.0
PAN/SWNT3	10	9.2	6.8 ± 0.7	93 ± 9	4.3 ± 1	243.0
PAN/SWNT4	10	9.2	6.4 ± 1.3	74 ± 28	1.6 ± 0.9	37.6
PAN/SWNT5	10	9.2	5.6 ± 0.4	56 ± 11	1.3 ± 0.5	30.0
PAN/DWNT	10	8.0	4.4 ± 0.6	64 ± 10	1.9 ± 0.6	5.9
PAN/MWNT	10	6.8	3.6 ± 0.3	56 ± 9	2.1 ± 0.6	1.5
PAN/VGCNF	10	6.3	4.1 ± 0.3	73 ± 6	3.7 ± 0.5	35.2
PAN/SWNT1	20	18.5	4.9 ± 0.3	72 ± 9	1.9 ± 0.3	2.7×10^2
PAN/SWNT3	20	18.5	9.3 ± 0.7	102 ± 8	3.6 ± 0.6	5.5×10^3
PAN/SWNT5	20	18.5	7.0 ± 1.1	66 ± 22	1.8 ± 0.7	1.3×10^2
PAN/VGCNF	20	13.1	4.0 ± 0.2	59 ± 3	2.5 ± 0.3	88.8

from the PAN/CNT films in this work are in agreement with Cadek on poly(vinyl alcohol)/CNT systems (10).

Dynamic Mechanical Properties of PAN/CNT Composite Films. The storage modulus (E') and tan δ curves of control PAN and PAN/CNT (5 wt %) composite films are shown in Figure 4. The storage modulus (E') and tan δ curves for 10 and 20 wt % PAN/CNT composite films are shown in the Supporting Information, Figures S5−S6. Storage modulus and tan δ curve for the 10 and 20 wt % composites show are similar trends to those in Figure 4. Tan δ peak temperatures for PAN/CNT composite films in general are higher than that of the PAN films. Moderate enhancement in storage modulus are obtained for PAN/SWNT2, PAN/SWNT3 PAN/SWNT4, PAN/MWNT, and PAN/VGCNF composites at 5 wt % CNT loading, below the glass transition temperature (T_g). At 25 °C, PAN/SWNT3 exhibits the highest enhancement in storage modulus (1.7 times that of the control PAN). However, no improvement in storage modulus is observed for PAN/SWNT1, PAN/SWNT5, and PAN/DWNT composites.

Enhancement in storage modulus for the composite films is significantly higher above the T_g. The highest increase in storage modulus above T_g is observed for 5 and 10 wt % PAN/SWNT3 films, followed by PAN/SWNT4, PAN/SWNT5, and PAN/SWNT2 composites. The storage modulus at 125 °C is about 14, 27, and 31 times that of the control PAN for 5, 10, and 20 wt % PAN/SWNT3 films, respectively. For PAN/SWNT4, the improvement in storage modulus at 125 °C is 7 and 13 times that of control PAN for 5 and 10 wt % composites, respectively, whereas it is 5 and 9 times for PAN/SWNT2 at 5 and 10 wt % loadings, respectively.

For SWNT1 composite films at low loading, enhancement in storage modulus above T_g is considerably low as compared to SWNT2, SWNT3, SWNT4, and SWNT5; however, at higher CNT loading (20 wt %), significant enhancement in storage modulus (10 times that of control PAN at 125 °C) is observed. Storage modulus at 125 °C for PAN/DWNT, PAN/MWNT, and PAN/VGCNF is comparable for both 5 and 10 wt % CNT loading. However, enhancement is significantly less as compared to the PAN/SWNT3 composite film.

The tan δ peak typically shifts to higher temperature and its magnitude decreases for PAN/SWNT composites (11, 37). The highest reduction in magnitude of the tan δ peak is observed for the PAN/SWNT3 composite film at 5 wt % CNT loading (Figure 4); the tan δ magnitude decreased from ∼0.37 for control PAN to ∼0.2 for the PAN/SWNT3 composite. For the PAN/SWNT2 and PAN/SWNT4 composites, the magnitude of the tan δ peak is ∼0.25. For SWNT1 and SWNT5, the value of the tan δ peak height is ∼0.3. At 5 wt % loadings, PAN/VGCNF composites show no appreciable reduction in tan δ magnitude (Figure 4). Previously published work from this group on PAN/VGCNF films show similar tan δ behavior for 5 and 10 wt % loadings (46). For PAN/DWNT and PAN/MWNT, the magnitude of tan δ peak shows slight reduction to ∼0.3 (Figure 4). A similar trend in magnitude of the tan δ peak is observed for the composite films with 10 wt % loadings. Reduction in the tan δ peak magnitude for the PAN/CNT composites suggests suppression of polymer molecular motion, hence imparting more elastic behavior. This suppression of molecular motion can be considered a result of interaction between the polymer and CNT. Therefore, PAN/SWNT3 (5 wt %) composites exhibit the highest interaction as indicated by the highest reduction in magnitude of tan δ peak (Figure 4), and this trend was also observed at all other loadings (10 and 20 w%). The trend in tensile modulus, tensile strength, storage modulus, and

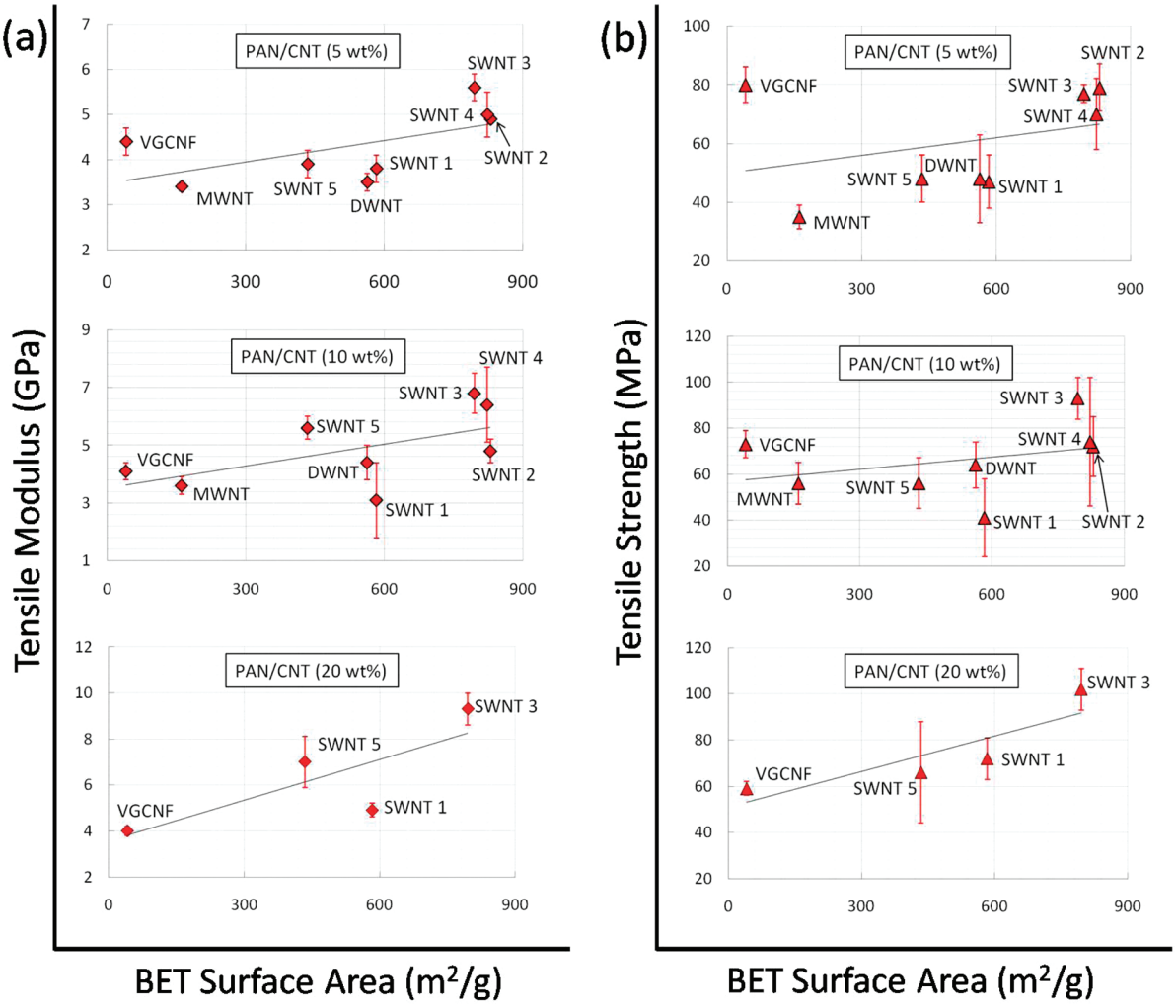

FIGURE 3. (a) Tensile modulus of control PAN and PAN/CNT composite films as a function of CNT surface area. Correlation was based on all the samples except sample number 8 (PAN/VGCNF). (b) Tensile strength of control PAN and PAN/CNT composite films as a function of CNT surface area. Correlation was based on all the samples except sample number 8 (PAN/VGCNF).

magnitude of tan δ peak for the PAN/CNT composites are in good qualitative agreement with each other.

The storage modulus of control PAN and various PAN/CNT films at different temperature are determined (Figure 5). The difference in storage modulus between the composite films and the control PAN film ($E'_{composite} - E'_{PAN}$) is plotted as a function of temperature in Figure 5. This analysis is a means to study the contribution of the CNT materials in the composites and also give some insight in PAN-CNT interfacial interaction. It is expected that above T_g, the polymer expands more rapidly as compared to more dimensionally stable nanotubes. For this reason, the contact forces between the polymer and nanotubes are expected to decrease as the temperature is raised. Hence polymer−nanotube slippage may occur at high temperatures causing the modulus difference to decrease (67−69). In this work, the modulus difference ($E'_{composite} - E'_{PAN}$) for DWNT, MWNT, and VGCNF composite films decrease to approximately zero above T_g denoting complete slippage of CNT from the polymer matrices (no CNT contribution to the modulus) (Figure 5). For the PAN/SWNT composites, the values for SWNT samples were varied from 0.2 GPa (SWNT1 5 wt %) to 1.4 GPa (SWNT3 20 wt %) showing better interaction of SWNT with PAN at the interfaces. Improvement in PAN−CNT interfacial interaction may be due to smaller tube diameter and the increase in CNT surface area for these samples. Similar studies of temperature-dependent modulus contribution from CNT have been reported for epoxy/CNT (70), PAN/CNT (71), and polypropylene/CNT (72) composites. A better understanding of the observed phenomenon is required for designing polymer−nanotube interfaces, and to achieve efficient load transfer between the nanotube matrix.

The tan δ curves from dynamic mechanical analysis of the films performed at frequencies of 0.1, 1, 5, and 10 Hz were used for activation energy calculations. On the basis of the tan δ curves, the T_g is determined for the composite films, which is evidence for PAN molecular motion. Activation energy for the composite at this transition (T_g) is indicative to the level of physical interaction between the PAN and CNT. Using conventional Arrhenius analysis, eq 2 was used to determine the activation energy; the values are listed in Table 4.

$$f = A\exp\left(-\frac{E_A}{RT}\right) \qquad (2)$$

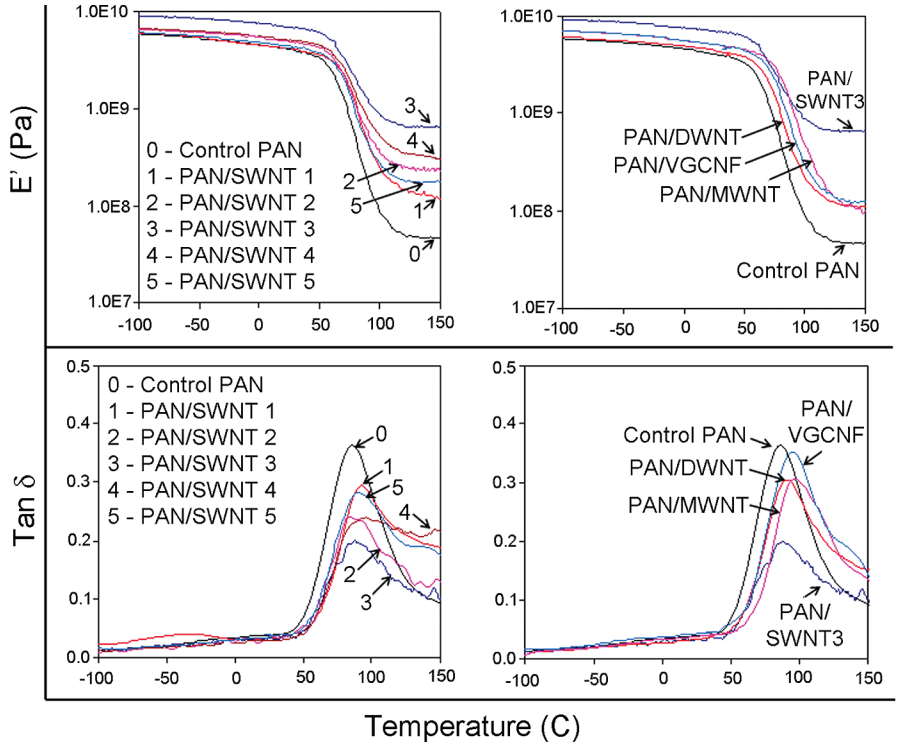

FIGURE 4. Storage modulus (E') and tan δ versus temperature plots of various PAN/CNT composite films with 5 wt % CNT loading.

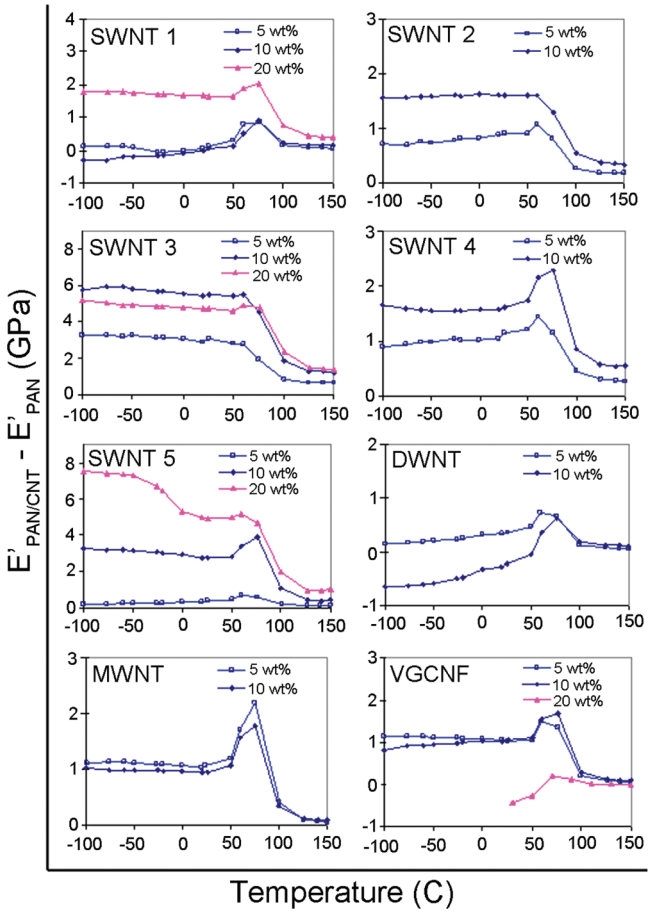

FIGURE 5. Storage modulus (E') difference between PAN/CNT films and control PAN film as a function of temperature.

Where E_A is the activation energy, f, R, and T are frequency, gas constant, and absolute temperature, respectively. The activation energies for the PAN molecular motion in the various films are compared in Figure 6a. As compared to the control PAN films, increases in E_A signify of interaction between the polymer and the nanotubes. At 5 wt % CNT loading, the activation energy of PAN/SWNT3 is 2.3 times that for the PAN film. Meanwhile, at the same loading, the increase in activation energy for PAN/SWNT1 and PAN/SWNT2 is 1.6 and 2.0 times that of the control PAN, respectively. For composites with 10 wt % nanotube loading, activation energy enhancement is the largest for PAN/SWNT3, followed by PAN/SWNT1, PAN/SWNT4, PAN/SWNT2, and PAN/SWNT5. For composites containing 20 wt % CNT, the increase in activation energy for PAN/SWNT5 is larger than that for PAN/SWNT1 and PAN/SWNT3 composites. At both 5 and 10 wt % loadings, activation energy for PAN/MWNT composite films shows no significant change as compared to the control PAN (Figure 6a and Table 4). E_A among the composites show that PAN−CNT interaction varies, and this may be based on several factors, which include CNT loading, structure and morphology of the tubes, dispersion of the CNT in the composite, as well as impurities present in the CNT samples.

Thermal Properties of PAN/CNT Composite Films. Dimensional change in PAN/CNT composites as a function of temperature are measured and classified based on different slopes of the curve for films. The curve is divided into three regions, as shown in Figure 6b (taking the control PAN and PAN/SWNT1 composite films with 10 wt % loading as examples). The temperatures at which slope of the curves change are the transition temperatures, named as the first transition temperature (T_I) and second transition temperature (T_{II}), respectively, and are listed in Table 4. The coef-

Table 4. Dynamic and Thermomechanical Analysis Results for Control PAN Film and Various PAN/SWNT Composite Films

sample	CNT loading (wt %)	activation energy (kJ/mol)	T_g[a] (°C)	transition temperatures[b] (°C)		CTE (× 10^{-6}/°C)		
				T_I	T_{II}	region I	region II	region III
control PAN	0	425	88	75	99	55	91	60
PAN/SWNT1	5	659	94	67	101	35	59	43
PAN/SWNT2	5	843	89	70	109	24	51	28
PAN/SWNT3	5	969	89	64	103	18	30	9
PAN/SWNT4	5	476	96	65	105	19	41	12
PAN/SWNT5	5	479	90	69	105	30	46	17
PAN/DWNT	5	457	92	74	103	41	66	45
PAN/MWNT	5	400	98	67	101	37	63	32
PAN/VGCNF	5	754	96	72	99	39	72	58
PAN/SWNT1	10	1011	92	71	100	32	59	53
PAN/SWNT2	10	1006	90	68	100	23	35	17
PAN/SWNT3	10	1343	92	65	93	11	20	6
PAN/SWNT4	10	1069	102	66	95	18	26	16
PAN/SWNT5	10	619	104	66	98	17	29	16
PAN/DWNT	10	913	92	68	106	28	47	48
PAN/MWNT	10	438	94	71	102	29	55	40
PAN/VGCNF	10	538	94	72	99	36	61	54
PAN/SWNT1	20	434	98	74	97	22	33	44
PAN/SWNT3	20	526	108	65	98	7	9	4
PAN/SWNT5	20	892	103	78	96	14	20	18

[a] T_g is determined by DMA at a frequency of 1 Hz. [b] Transition temperatures are determined by TMA. T_I, the first transition temperature; T_{II}, the second transition temperature.

ficient of thermal expansion (CTE) in all three regions for various films were determined and are listed in Table 4. All PAN/CNT composite films exhibit reduced thermal expansion as compared to the control PAN film. The CTE values for the control PAN film are 55 × 10^{-6} K^{-1}, 91 × 10^{-6} K^{-1}, and 60 × 10^{-6} K^{-1} in regions I, II, and III, respectively. At 5 wt % CNT loading, PAN/SWNT3 shows the highest reduction in CTE relative to the control PAN (CTE reduced from 55 × 10^{-6} K^{-1} for control PAN to 18 × 10^{-6} K^{-1} (region I), a reduction in CTE of about 67%). PAN/SWNT4 films show the next highest reduction in CTE followed by PAN/SWNT5, PAN/SWNT2, PAN/SWNT1, PAN/MWNT, PAN/DWNT, and PAN/VGCNF. Similar trends in CTE reduction are shown for composites with 10 wt % (except for PAN/MWNT) and 20 wt % CNT loadings. These values are higher than CTE reported for PAN/SWNT (60/40) films with 1.7 × 10^{-6} K^{-1} and 0.6 × 10^{-6} K^{-1} below and above T_g, respectively (47).

Xu et al. (73) reported a decrease in CTE of PVDF/SWNT composite by 35 wt % and at 49 wt % nanotube loading. In our case, CTE of the PAN/SWNT3 composite film with only 20 wt % loading is reduced by 90% as compared to the control PAN, indicating good polymer−nanotube interaction. It is noteworthy that for various PAN/SWNT composites, the trend for reduction in CTE follows a similar order as that for enhancement in tensile and dynamic mechanical properties. PAN/VGCNF composite films show the lowest reduction in CTE as compared to other composite films, indicating relatively poor interaction between PAN and VGCNF, which is also evident by the SEM images of tensile fractured film surfaces (46). Analysis of CTE values for various PAN/CNT composites in regions I, II, and III show that CTE decreases with increasing CNT surface area (see the Supporting Information, Figure S7).

Raman Spectra of PAN/CNT Composite Films. Radial breathing mode (RBM) bands in Raman spectra for CNT powders and various composite films were fitted with Lorentzian components (Figure 7) (see also the Supporting Information, Figure S8). Each component corresponds to certain nanotube diameter which can be calculated from the frequencies of the RBM bands (74). For SWNT1, SWNT2, SWNT3, and DWNT powders and their composite films, RBM peaks were fitted with two Lorentzian components located at 263 and 267 cm^{-1} (Figure 7). For SWNT4 powder and PAN/SWNT4 composite films, RBM band was fitted with three Lorentzian components located at 235, 263, and 267 cm^{-1}, whereas the RBM band for SWNT5 powder and PAN/SWNT5 films was fitted with three Lorentzian components located at 233, 263, and 267 cm^{-1}. The peaks located at 233, 235, 263, and 267 cm^{-1} correspond to the nanotube diameters of 1.01, 1.00, 0.89, and 0.88, respectively. At 785 nm laser excitation, not all CNT diameters, chirality, and metallic tubes can be observed for the samples used in the current work.

RBM peak intensity varies for the composite films as compared to the CNT powders (Figure 7). RBM intensity depends on the laser excitation energy (E_{laser}). Under strain, the energy separation between the van Hove singularities, E_{ii} shifts closer to or farther away from laser excitation energy (E_{laser}). When the difference $|E_{ii} - E_{laser}|$ decreases, RBM intensity increases and vice versa. RBM intensity reaches a maximum when $E_{ii} = E_{laser}$. The second-order energy separation, E_{22}^{S}, for the semiconducting nanotube for

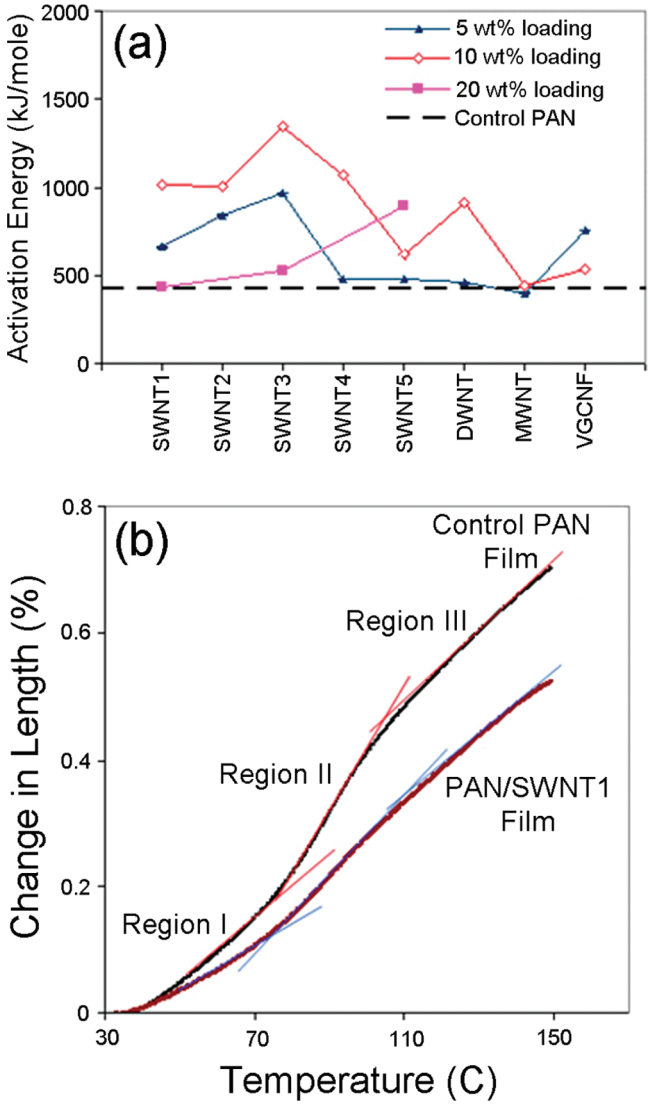

FIGURE 6. (a) Activation energy for the PAN T_g in control PAN and various PAN/CNT composite films. Dashed line represents the activation energy for control PAN films which is independent of CNT. (b) Thermal expansion as a function of temperature for control (a) PAN and (b) PAN/SWNT1 (90/10) composite films.

the 263 cm^{-1} peak is in the range of 1.81−1.88 eV (75). Under compressive stress, the E_{22}^{S} value for the 263 cm^{-1} peak increases (mode 1) (76) and shifts farther away from the laser energy value of 1.58 eV, resulting in decreased intensity. PAN/SWNT and PAN/DWNT composites do show the decreased intensity of peak at 263 cm^{-1} as compared to CNT powders (Figure 7).

The E_{22}^{S} value of the 267 cm^{-1} peak is between 1.81 and 1.90 eV (75). Under compressive stress, the E_{22}^{S} value of the 267 cm^{-1} peak decreases (mode 2) (76), shifts closer to E_{laser}, and results in increased intensity (75, 76). PAN/SWNT5 composite films exhibit increased intensity of 267 cm^{-1} peak (Figure 7). However, the intensity for the 267 cm^{-1} peak decreased for PAN/SWNT1, PAN/SWNT3, PAN/SWNT4, and PAN/DWNT composite films (Figure 7). PAN/SWNT2 composites show no significant change compared to their corresponding CNT powders. The reason for this decreased intensity is not clear. As mentioned previously, all intensities

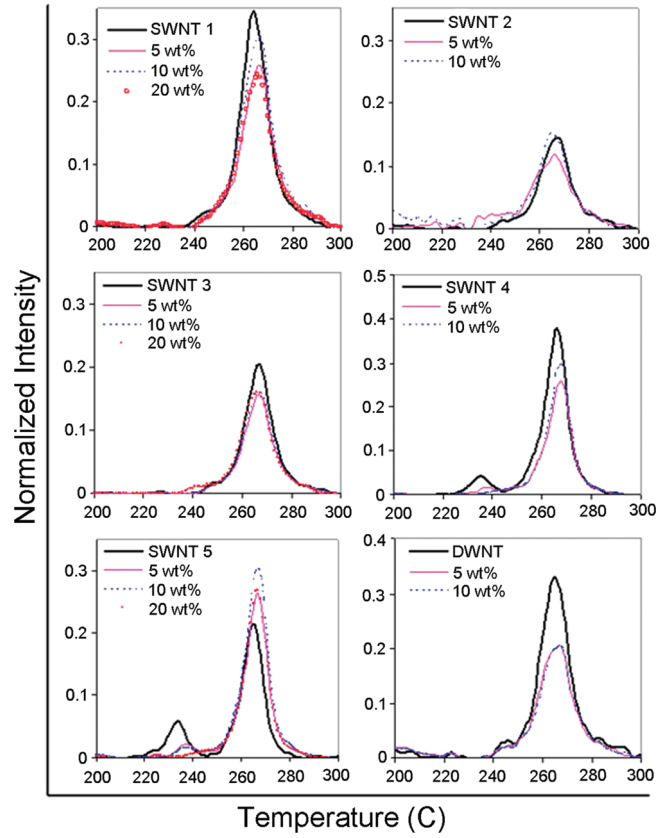

FIGURE 7. Radial breathing mode (RBM) of Raman spectra for DWNT, various SWNTs, and their corresponding composite films.

have been normalized linearly taking the intensity of the G-band as unity.

The intensity of the peak at 235 cm^{-1} decreased for PAN/SWNT4 composite films as compared to that for the SWNT4 powder. With increase in SWNT4 loading, 235 cm^{-1} peak intensity for composite films further decreases. This intensity variation comes from the effect of strain exerted by PAN molecules on resonance. Under compressive strain, the E_{22}^{S} value of the 235 cm^{-1} peak located in the range of 1.59−1.67 eV will decrease (mode 2) and shifts to closer to the laser energy (75, 76). Normalized 235 cm^{-1} peak intensities for the PAN/SWNT5 composite film are suppressed as compared to that for the SWNT5 powder and decrease with increasing SWNT5 loading (Figure 7).

For SWNT1, SWNT4, SWNT5, and DWNT containing composite films, the RBM peak positions show a slight upshift to higher frequency as compared to their respective CNT powders (Figure 7). The RBM peak positions for the other composite films show no significant difference relative to their CNT powders. Calculation of the pressure dependence of RBM position showed that RBM position increase approximately linearly with increasing pressure (77). The upshift of RBM for various PAN/CNT films may also be due to the compressive force exerted by the PAN molecules on the nanotube bundles.

G band positions, fwhm of G band, and G′ band position (at ∼2585 cm^{-1}) for CNT powders and various PAN/CNT composite films were observed from Raman spectroscopy. No significant shift of G band position is observed for PAN/

Table 5. Structural Properties and Density of Control PAN and PAN/CNT Composite Films

sample	CNT loading (wt %)	CNT loading (vol %)	PAN crystallinity (%)	PAN cryst size (nm)	experimental density (g/cm^3)	theoretical density[a] (g/cm^3)
control PAN	0	0	43	5.7	1.15 ± 0.06	1.18
PAN/SWNT1	5	4.6	48	4.9	0.89 ± 0.05	1.19
PAN/SWNT2	5	4.6	47	5.2	0.97 ± 0.04	1.19
PAN/SWNT3	5	4.6	46	5.1	1.00 ± 0.01	1.19
PAN/SWNT4	5	4.6	46	4.8	0.98 ± 0.01	1.19
PAN/SWNT5	5	4.6	48	5.1	0.97 ± 0.02	1.19
PAN/DWNT	5	4.0	48	5.4	0.88 ± 0.01	1.19
PAN/MWNT	5	3.3	50	5.4	0.95 ± 0.01	1.20
PAN/VGCNF	5	3.1	49	5.4	1.22 ± 0.07	1.20
PAN/SWNT1	10	9.2	47	5.2	0.68 ± 0.01	1.19
PAN/SWNT2	10	9.2	46	5.2	0.92 ± 0.03	1.19
PAN/SWNT3	10	9.2	45	4.9	1.08 ± 0.01	1.19
PAN/SWNT4	10	9.2	46	4.7	0.96 ± 0.09	1.19
PAN/SWNT5	10	9.2	49	5.0	0.98 ± 0.06	1.19
PAN/DWNT	10	8.0	46	4.9	0.87 ± 0.01	1.21
PAN/MWNT	10	6.8	50	5.4	0.88 ± 0.02	1.22
PAN/VGCNF	10	6.3	46	5.1	0.91 ± 0.09	1.23
PAN/SWNT1	20	18.5	41	4.8	0.93 ± 0.02	1.20
PAN/SWNT3	20	18.5	38	4.5	1.03 ± 0.01	1.20
PAN/SWNT5	20	18.5	41	4.8	1.08 ± 0.03	1.20
PAN/VGCNF	20	13.1	43	5.9	0.66 ± 0.05	1.28

[a] Theoretical density of the composite films is calculated using the equation $\rho_c = V_f(\rho_f - \rho_m) + \rho_m$, where ρ_c is the density of the composite film; V_f is the volume fraction of filler; ρ_m is the density of PAN (1.18 g/cm^3); ρ_f is the density of filler SWNT (1.3 g/cm^3) (80), DWNT (1.5 g/cm^3) (81), MWNT (1.8 g/cm^3) (82), and VGCNF (1.95 g/cm^3) (82).

CNT composite films (except for the PAN/SWNT1 composites), as compared to the G band of their CNT powder, whereas fwhm decreases in composite films with an increase in nanotube loading for most CNT. An upshift of the G′ band is observed for the PAN/CNT composite films except for PAN/MWNT and PAN/VGCNF films. In PAN/MWNT and PAN/VGCNF films, the excitation from laser occurs only at the outer walls of the tubes, resulting in no shift in G′ band position. The upshift of G band and G′ band in polymer/CNT composites is attributed to the compressive force on the nanotubes exerted by the polymer (78). The G′ band is more sensitive to the pressure as compared to the G band, resulting in larger band position shift (79).

Solvent Resistance of PAN/CNT Composite Films. PAN/CNT composite films with 10 wt % CNT loading were immersed in DMF for 1 h at room temperature (25 °C) (see the Supporting Information, Figure S9). Various PAN/SWNT composite films remain intact and retained their shapes indicating strong interaction between PAN and SWNT. For the PAN/SWNT1, PAN/SWNT4, and PAN/SWNT5 composite films, no obvious disintegration is observed, indicating that no significant amount of SWNT material is removed because of the addition of solvent. Of the five PAN/SWNT films, PAN/SWNT2 and PAN/SWNT3 composites shows the least solvent resistance, as indicated by the removal of SWNT material from the films. Mechanical and electrical properties and thermal expansion results for various PAN/SWNT composite films indicate that the interaction between PAN and SWNT3 is better. Hence, the results from solvent-resistance of PAN/SWNT3 films are contrary to what is expected on the basis of mechanical properties measured. In the case of PAN/DWNT, PAN/MWNT, and PAN/VGCNF composite films, solvent resistance in lower than that exhibited by the various PAN/SWNT films. These films disintegrate more readily and imply that PAN interaction with DWNT, MWNT, and VGCNF is weaker than PAN−SWNT interaction. The solvent study does confirm that all SWNT exhibit better interaction with PAN than do DWNT, MWNT, and VGCNF.

Structure and Morphology of PAN/CNT Composite Films. WAXD patterns for various films are measured and analyzed. PAN crystallite size calculated using Scherrer equation from the (110) peak at ∼16.8° 2θ, and PAN X-ray crystallinity values are given in Table 5. PAN crystallinity increases by the addition of CNT. PAN crystal size determined from (110) peaks in the composite films is smaller than that in the control PAN film. PAN crystallinity and crystal size are the largest in the composite film containing MWNT. SEM images of various CNT powder showed MWNT and VGCNF exist as individual nanotubes while SWNT form bundles. MWNT, SWNT, and DWNT are more entangled. Morphologies of the fractured cross-section of the various PAN/CNT (10 wt %) composite films were observed by SEM. CNTs are well-dispersed in the PAN matrix except for DWNT. Previous results from this group for PAN/DWNT fibers show that DWNTs exhibit poor dispersion and are highly entangled (11). During preparation of composite films, DWNT was the most difficult to disperse in the solvent. Though more sonication time is used to disperse DWNTs, its dispersion quality in the polymer is not very good. The SEM images

do not show any significant difference in the dispersion quality of various SWNTs in the PAN matrix.

CONCLUSIONS

Polyacrylonitrile composite films of about 25 μm thickness have been processed using eight different types of carbon nanotubes at nanotube loadings of 5, 10, and 20 wt %. Generally, tensile modulus and tensile strength of PAN/CNT composites increased, whereas coefficient of thermal expansion decreased with increasing CNT surface area. Dynamic mechanical properties of the composite films have been measured and compared to those of the control PAN. In-plane dc electrical conductivity and film solvent resistance in DMF was also characterized. On the basis of these studies, it is concluded that in general DWNT, MWNT, and VGCNF exhibit relatively poor interaction with PAN when compared to SWNT used in this study. However, different SWNT samples were observed to have variable interaction with PAN depending on metallic impurity, surface area, and diameter. Using Raman Spectroscopy, RBM, D, G, and G′ bands have been analyzed and discussed for various CNT and PAN/CNT composite films. Structure and morphology of the films have been examined by SEM and WAXD. Among all composites, PAN/SWNT3 exhibits the highest improvement in tensile modulus, storage modulus, electrical conductivity, and most reduction in thermal shrinkage. The study also shows how CNT structure and morphology can affect the overall properties of polymer−CNT composites.

Acknowledgment. The work was supported by AFOSR.

Supporting Information Available: Additional tables and figures as they pertain to the work outlined in this article (PDF). This material is available free of charge via the Internet at http://pubs.acs.org.

REFERENCES AND NOTES

(1) Chae, H. G.; Minus, M. L.; Kumar, S. *Polymer* **2006**, *47* (10), 3494–3504.
(2) Chae, H. G.; Minus, M. L.; Rasheed, A.; Kumar, S. *Polymer* **2007**, *48* (13), 3781–3789.
(3) Minus, M. L.; Chae, H. G.; Kumar, S. *Polymer* **2006**, *47* (11), 3705–3710.
(4) Minus, M. L.; Chae, H. G.; Kumar, S. *Macromol. Chem. Phys.* **2009**, *210* (21), 1799–1808.
(5) Wei, C. Y. *Nano Lett.* **2006**, *6* (8), 1627–1631.
(6) Czerw, R.; Guo, Z. X.; Ajayan, P. M.; Sun, Y. P.; Carroll, D. L. *Nano Lett.* **2001**, *1* (8), 423–427.
(7) Peijs, T.; Vanvught, R. J. M.; Govaert, L. E. *Composites* **1995**, *26* (2), 83–90.
(8) Potschke, P.; Brunig, H.; Janke, A.; Fischer, D.; Jehnichen, D. *Polymer* **2005**, *46* (23), 10355–10363.
(9) Prashantha, K.; Soulestin, J.; Lacrampe, M. F.; Krawczak, P. *Polym. Polym. Compos.* **2009**, *17* (4), 205–245.
(10) Cadek, M.; Coleman, J. N.; Ryan, K. P.; Nicolosi, V.; Bister, G.; Fonseca, A.; Nagy, J. B.; Szostak, K.; Beguin, F.; Blau, W. J. *Nano Lett.* **2004**, *4* (2), 353–356.
(11) Chae, H. G.; Sreekumar, T. V.; Uchida, T.; Kumar, S. *Polymer* **2005**, *46*, 10925–10935.
(12) Ryan, K. P.; Cadek, M.; Nicolosi, V.; Blond, D.; Ruether, M.; Armstrong, G.; Swan, H.; Fonseca, A.; Nagy, J. B.; Maser, W. K.; Blau, W. J.; Coleman, J. N. *Compos. Sci. Technol.* **2007**, *67* (7−8), 1640–1649.
(13) Dalton, A. B.; Collins, S.; Munoz, E.; Razal, J. M.; Ebron, V. H.; Ferraris, J. P.; Coleman, J. N.; Kim, B. G.; Baughman, R. H. *Nature* **2003**, *423* (6941), 703.
(14) Ciselli, P.; Wang, Z.; Peijs, T. *Mater. Technol.* **2007**, *22* (1), 10–21.
(15) Coleman, J. N.; Cadek, M.; Ryan, K. P.; Fonseca, A.; Nagy, J. B.; Blau, W. J.; Ferreira, M. S. *Polymer* **2006**, *47* (26), 8556–8561.
(16) Green, M. J.; Behabtu, N.; Pasquali, M.; Adams, W. W. *Polymer* **2009**, *50* (21), 4979–4997.
(17) Miyagawa, H.; Misra, M.; Mohanty, A. K. *J. Nanosci. Nanotechnol.* **2005**, *5* (10), 1593–1615.
(18) Coleman, J. N.; Khan, U.; Blau, W. J.; Gun'ko, Y. K. *Carbon* **2006**, *44* (9), 1624–1652.
(19) Dondero, W. E.; Gorga, R. E. *J. Polym. Sci., Part B: Polym. Phys.* **2006**, *44* (5), 864–878.
(20) Khan, U.; Ryan, K.; Blau, W. J.; Coleman, J. N. *Compos. Sci. Technol.* **2007**, *67* (15−16), 3158–3167.
(21) Bauhofer, W.; Kovacs, J. Z. *Compos. Sci. Technol.* **2009**, *69*, 1486–1498.
(22) Peng, H. S.; Sun, X. M. *Chem. Phys. Lett.* **2009**, *471* (1−3), 103–105.
(23) Ramasubramaniam, R.; Chen, J.; Liu, H. Y. *Appl. Phys. Lett.* **2003**, *83* (14), 2928–2930.
(24) Chen, Y.; Lin, Y.; Liu, Y.; Doyle, J.; He, N.; Zhuang, X. D.; Bai, J. R.; Blau, W. J. *J. Nanosci. Nanotechnol.* **2007**, *7* (4−5), 1268–1283.
(25) Kymakis, E.; Alexandou, I.; Amaratunga, G. A. J. *Synth. Met.* **2002**, *127*, 59–62.
(26) Vaisman, L.; Wagner, H. D.; Marom, G. *Adv. Colloid Interface Sci.* **2006**, *128*, 37–46.
(27) Hussain, F.; Hojjati, M.; Okamoto, M.; Gorga, R. E. *J. Compos. Mater.* **2006**, *40* (17), 1511–1575.
(28) Du, J. H.; Bai, J.; Cheng, H. M. *Express Polym. Lett.* **2007**, *1* (5), 253–273.
(29) Cooper, C. A.; Ravich, D.; Lips, D.; Mayer, J.; Wagner, H. D. *Compos. Sci. Technol.* **2002**, *62* (7−8), 1105–1112.
(30) Jiang, L. Y.; Tan, H. L.; Wu, J.; Huang, Y. G.; Hwang, K. C. *Nano* **2007**, *2* (3), 139–148.
(31) Donnet, J. B.; Bansal, R. C. *Carbon Fibers*.; Marcel Dekker: New York, 1984.
(32) Donnet, J.-B.; Wang, T. K.; Rebouillat, S.; Peng, J. C. *Carbon Fibers*, 3rd ed.; Marcel Dekker: New York, 1998.
(33) Jagannathan, S.; Chae, H. G.; Jain, R.; Kumar, S. *J. Power Sources* **2008**, *185* (2), 676–684.
(34) Ra, E. J.; Raymundo-Pinero, E.; Lee, Y. H.; Beguin, F. *Carbon* **2009**, *47* (13), 2984–2992.
(35) Ma, G. P.; Yang, D. Z.; Nie, J. *Polym. Adv. Technol.* **2009**, *20* (2), 147–150.
(36) Shen, X. Y.; Ji, Y. L.; Wang, J. *J. Appl. Polym. Sci.* **2008**, *110* (1), 313–320.
(37) Sreekumar, T. V.; Liu, T.; Min, B. G.; Guo, H.; Kumar, S.; Hauge, R. H.; Smalley, R. E. *Adv. Mater.* **2004**, *16* (1), 58–61.
(38) Kim, S. H.; Min, B. G.; Lee, S. C.; Park, S. B.; Lee, T. D.; Park, M.; Kumar, S. *Fibers Polym.* **2004**, *5* (3), 198–203.
(39) Chae, H. G.; Choi, Y. H.; Minus, M. L.; Kumar, S. *Compos. Sci. Technol.* **2009**, *69* (3−4), 406–413.
(40) Jagannathan, S.; Liu, T.; Kumar, S. *Compos. Sci. Technol.* **2010**, *70*, 593−598.
(41) Liu, T.; Sreekumar, T. V.; Kumar, S.; Hauge, R. H.; Smalley, R. E. *Carbon* **2003**, *41*, 3.
(42) Zhou, C. F.; Liu, T.; Wang, T.; Kumar, S. *Polymer* **2006**, *47* (16), 5831–5837.
(43) Wang, B.; Wang, H. P.; Hong, B.; Zhang, Y. *Polym. J.* **2005**, *37* (5), 376–379.
(44) Ge, J. J.; Hou, H. Q.; Li, Q.; Graham, M. J.; Greiner, A.; Reneker, D. H.; Harris, F. W.; Cheng, S. Z. D. *J. Am. Chem. Soc.* **2004**, *126* (48), 15754–15761.
(45) Khenoussi, N.; Drean, E.; Schacher, L.; Adolphe, D. C.; Balard, H. *Mater. Technol.* **2009**, *24* (1), 36–40.
(46) Guo, H.; Rasheed, A.; Minus, M.; Kumar, S. *J. Mater. Sci.* **2008**, *43* (13), 4363–4369.
(47) Guo, H.; Sreekumar, T. V.; Liu, T.; Minus, M. L.; Kumar, S. *Polymer* **2005**, *48*, 3001–3005.
(48) Kim, S. H.; Min, B. G.; Lee, S. C. *Fibers Polym.* **2005**, *6* (2), 108–112.
(49) Koganemaru, A.; Bin, Y.; Agari, Y.; Matsuo, M. *Adv. Funct. Mater.* **2004**, *14* (9), 842–850.
(50) Koganemaru, A.; Bin, Y. Z.; Tohora, H.; Okino, F.; Komiyama, S.; Zhu, J.; Matsuo, M. *Asia-Pac. J. Chem. Eng.* **2008**, *3* (5), 521–526.

(51) Vast, L.; Rochez, O.; Azoulay, L.; Fonseca, A.; Nagy, J. B.; Deniau, G.; Palacin, S.; Delhalle, J.; Mekhalif, Z. *J. Nanosci. Nanotechnol.* **2007**, *7* (10), 3404–3410.
(52) Pirlot, C.; Mekhalif, Z.; Fonseca, A.; Nagy, J. B.; Demortier, G.; Delhalle, J. *Chem. Phys. Lett.* **2003**, *372* (3−4), 595–602.
(53) Pirlot, C.; Willems, I.; Fonseca, A.; Nagy, J. B.; Delhalle, J. *Adv. Eng. Mater.* **2002**, *4* (3), 109–114.
(54) Liu, J.; Rasheed, A.; Minus, M. L.; Kumar, S. *J. Appl. Polym. Sci.* **2009**, *112* (1), 142–156.
(55) Lee, G.-W.; Kumar, S. *J. Phys. Chem. B* **2005**, *109*, 17128–17133.
(56) Li, H. J.; Feng, L.; Guan, L. H.; Shi, Z. J.; Gu, Z. N. *Solid State Commun.* **2004**, *132* (3−4), 219–224.
(57) Uchida, T.; Anderson, D. P.; Minus, M. L.; Kumar, S. *J. Mater. Sci.* **2006**, *41* (18), 5851–5856.
(58) Kumar, S.; Anderson, D. P.; Crasto, A. S. *J. Mater. Sci.* **1993**, *28* (2), 423–439.
(59) Thess, A.; Lee, R.; Nikolaev, P.; Dai, H. J.; Petit, P.; Robert, J.; Xu, C. H.; Lee, Y. H.; Kim, S. G.; Rinzler, A. G.; Colbert, D. T.; Scuseria, G. E.; Tomanek, D.; Fischer, J. E.; Smalley, R. E. *Science* **1996**, *273* (5274), 483–487.
(60) Ergun, S., *Chemistry and Physics of Carbon*; Walker, P. L., Ed.; Marcel Dekker: New York, 1968; Vol. 3.
(61) Ruland, W., *Chemistry and Physics of Carbon*; Walker, P. L., Ed.; Marcel Dekker: New York, 1968; Vol. 4.
(62) Yen, T. F.; Erdman, J. G.; Pollack, S. S. *Anal. Chem.* **1961**, *33* (11), 1587.
(63) Lu, L.; Sahajwalla, V.; Kong, C.; Harris, D. *Carbon* **2001**, *39* (12), 1821–1833.
(64) Ra, E. J.; An, K. H.; Kim, K. K.; Jeong, S. Y.; Lee, Y. H. *Chem. Phys. Lett.* **2005**, *413* (1−3), 188–193.
(65) Ju, Y. W.; Choi, G. R.; Jung, H. R.; Lee, W. J. *Electrochim. Acta* **2008**, *53* (19), 5796–5803.
(66) Han, S. J.; Kim, B.; Suh, K. D. *Macromol. Chem. Phys.* **2007**, *208* (4), 377–383.
(67) Lee, B.-L.; Nielsen, L. E. *J. Polym. Sci.: Polym. Phys. Ed.* **1977**, *15* (4), 683–692.
(68) Nielsen, L. E., *Mechanical Properties of Polymers and Composites*; Marcel Dekker: New York, 1974; Vol. 2.
(69) Suhr, J.; Koratkar, N.; Keblinski, P.; Ajayan, P. *Nat. Lett.* **2005**, *4*, 134.
(70) Choi, Y. K.; Sugimoto, K.; Song, S. M.; Gotoh, Y.; Ohkoshi, Y.; Endo, M. *Carbon* **2005**, *43* (10), 2199–2208.
(71) Chae, H. G.; Kumar, S. *J. Appl. Polym. Sci.* **2006**, *100* (1), 791–802.
(72) Lee, G. W.; Jagannathan, S.; Chae, H. G.; Minus, M. L.; Kumar, S. *Polymer* **2008**, *49*, 1831–1840.
(73) Xu, Y. S.; Ray, G.; Abdel-Magid, B. *Compos., Part A* **2006**, *37* (1), 114–121.
(74) Bachilo, S. M.; Strano, M. S.; Kittrell, C.; Hauge, R. H.; Smalley, R. E.; Weisman, R. B. *Science* **2002**, *298* (5602), 2361–2366.
(75) Dresselhaus, M. S.; Eklund, P. C. *Adv. Phys.* **2000**, *49* (6), 705–814.
(76) Lucas, M.; Young, R. J. *Phys. Rev. B* **2004**, *69* (8), 085405.
(77) Kahn, D.; Lu, J. P. *Phys. Rev. B* **1999**, *60* (9), 6535–6540.
(78) Rasheed, A.; Dadmun, M. D.; Ivanov, I.; Britt, P. F.; Geohegan, D. B. *Chem. Mater.* **2006**, *18* (15), 3513–3522.
(79) Venkateswaran, U. D.; Gosselin, M. E.; Postek, B.; Masica, D. L.; Chen, G.; Gupta, R.; Eklund, P. C. *Phys. Status Solidi, B* **2003**, *235* (2), 364–368.
(80) Lu, J. P. *Phys. Rev. Lett.* **1997**, *79* (7), 1297–1300.
(81) Sugai, T.; Yoshida, H.; Shimada, T.; Okazaki, T.; Shinohara, H. *Nano Lett.* **2003**, *3* (6), 769–773.
(82) Reich, S.; Thomsen, C.; Ordejon, P. *Phys. Rev. B* **2002**, *65* (15), 155411.

AM100155X